

Article

Parameter Analysis of Savonius Hydraulic Turbine Considering the Effect of Reducing Flow Velocity

Jianjun Yao ^{1,*}, Fengshen Li ^{1,*}, Junhua Chen ², Zheng Yuan ³ and Wangeng Mai ¹

¹ College of Mechanical and Electrical Engineering, Harbin Engineering University, Harbin 150001, China; 18845635138@163.com

² College of Science and Technology, Ningbo University, Ningbo 315100, China; cjh@nit.net.cn

³ College of Shipbuilding Engineering, Harbin Engineering University, Harbin 150001, China; yuanzheng2016@hrbeu.edu.cn

* Correspondence: travisyao@126.com (J.Y.); liyunshen8888@163.com (F.L.)

Received: 14 November 2019; Accepted: 16 December 2019; Published: 19 December 2019



Abstract: The Savonius-type hydraulic turbine, mainly known for its good self-starting properties and simple structure, not only has energy capturing characteristics but also has a certain effect on flow velocity reduction. Aside from ensuring energy capture efficiency, studying the effects of parameters on the flow velocity reduction capacity is of great significance for the protection of mariculture, as it can reduce the damage to cages and fishes. In this study, a computational fluid dynamics method was carried out to investigate the hydrodynamic characteristics and variations in the wake of a turbine. The accuracy of the simulation results was verified by experimental comparison. Firstly, the velocity contours and vectors were studied in detail to reveal the mechanism of the flow velocity reduction effect. Secondly, the velocity attenuation coefficient and relative attenuation length were formulated by the variation rule of the velocity field to evaluate the turbine reduction strength and range. Finally, the power coefficient was considered to predict the performance of a turbine under different tip speed ratios, overlap ratios, blade curvatures, and blade numbers. The results showed that the turbine had an obvious flow velocity reduction effect in the rear “sword”-shaped area, where the velocity field distribution had a certain regularity. In addition, by comprehensively comparing the simulation data, it was found that the respective effect trend of tip speed ratio, blade number, overlap ratio, and curvature on the turbine’s energy capture and flow velocity reduction characteristics was basically the same. Considering the effect of reducing flow velocity, a two-bladed turbine with a blade curvature of 0.8 and an overlap ratio of 0.15 is the optimal configuration.

Keywords: Savonius-type hydrokinetic turbine; basic parameters; flow velocity reduction; power-efficient; computational fluid dynamics

1. Introduction

At this stage of rapid social and economic development, the energy crisis and environmental damage caused by traditional fossil resources are becoming increasingly prominent. Tidal power, as a renewable energy source, has the characteristics of large reserves, high energy density, and small environmental impact [1]. According to their structural characteristics, tidal energy capture devices can be divided into three categories: Vertical axis, horizontal axis, and oscillating hydrofoil. The vertical axis Savonius turbine was first invented by the Finnish engineer Savonius [2]. Aside from its previous applications in wind power generation, it has also recently been widely used in the field of tidal power [3]. As a resistance-type vertical axis turbine, the Savonius hydrokinetic turbine (SHT) has a simple structure that is easy manufacture, good starting characteristics, and high dynamic moments [4]. It has no limit on flow direction and presents low noise and wear on moving parts.

Although the maximum power coefficient of resistance-type turbines is not high [5], they generate torque by the difference of drag forces working on the two blades formed by blocking the incoming flow, which results in an obvious flow velocity reduction effect. Recently, with the continuous development of mariculture techniques, concepts, such as deep-sea aquaculture fisheries and marine pastures have been proposed. Thus, cages have been evolving toward the open sea and at a large scale [6]. In the deep sea, there are general phenomena of strong winds, high waves, and rapid flow, which can easily damage breeding facilities and marine organisms. Especially for the widely used gravity cage, the deformation and stress concentration on the frame and netting caused by rapid flow rates greatly impact the effective cultivation volume and service life of the cage [7,8]. Hence, the placement of an SHT on the periphery of an aquaculture farm can both harvest energy for power facilities and reduce the flow velocity to protect the cages. Varying the tip speed ratio (*TSR*) and design parameters (overlap ratio, blade number, and blade curvature) of an SHT to enhance the flow velocity reduction property without compromising the power-efficiency has the potential to improve marine aquaculture greatly.

In the past decades, numerous experimental and numerical methods have been carried out to investigate the basic geometry parameters, auxiliary structure, and turbine combination forms to improve the stability and power harvesting efficiency of the Savonius rotor. Talukdar Parag K. et al. [9] studied the effect of several different basic parameters on the power generation efficiency of the SHT through simulations and experiments. Comparing the properties of different configurations proved that a two-bladed semicircular SHT with an overlap ratio of 0.15 and an aspect ratio of 0.7 achieved the maximum power coefficient of 0.28 at a *TSR* of 0.89. Saha U.K. et al. [10] experimentally studied the aerodynamic performance of different stages, blade numbers, and shapes of the Savonius rotor and found that the two-stage turbine with two twisted blades was the best. Tian Wenlong et al. [11] found that the straight-bladed Savonius wind turbine with a curvature of 0.72 had optimal power generation performance. Kamoji M.A. et al. [12] tested a Savonius wind rotor with a helical (or twisted) blade. It was found that the maximum power coefficient was around 0.174 when the helical Savonius rotor had no shaft and an overlap ratio of zero, and the self-starting property was also improved. Kumar A. et al. [13] reported the enhancement of energy capture efficiency by changing the section profile shape of the twisted Savonius rotor. Tian Wenlong et al. [14] proposed a modified Savonius wind turbine with novel blade shapes, which had a 10.98% performance improvement compared with a conventional Savonius turbine. Kerikous E. et al. [15] introduced 12 geometrical parameters to describe the shape of the blade. The full property potential of the SHT was investigated by coupling computational fluid dynamics (CFD) with the in-house flow optimizer OPALL. Kailash G. et al. [16] effectively reduced the generation of negative moments by placing a baffle at a suitable position on the front of the Savonius rotor. Irabu K. et al. [17] designed a guide-box tunnel with an inlet and movable outlet wall for augmenting the low wind velocity and protecting the turbine from strong wind damage. Tartuferi M. and D'Alessandro V. [18] proposed an innovative blade shape based on a cambered airfoil section and a conveyor-deflector curtain system that can self-adjust relative to the wind direction. The results confirmed that both of the adopted guidelines enhanced the overall performance of the Savonius wind rotor. Tang Z.P. et al. [19] proposed an omnidirectional deflector that increased the maximum power coefficient by around 48% under specific parameters. Ostos I. et al. [20] improved turbine performance by adding quarter blades to the classic Savonius device that do not require complex and expensive changes. Gupat R. [21] proved that a three-bladed Savonius rotor combined with a three-bladed Darrieus rotor provided greater efficiency than a simple Savonius rotor.

Investigations of the hydrodynamic characteristics of the SHT have been conducted by scholars [10–18]. However, research on the influence of a turbine on the wake velocity field has not been attempted. Thus, in this study, a two-dimensional CFD simulation method verified by a flume test was applied to examine the flow velocity reduction and energy capture properties of an SHT under different parameters. Based on the simulation results, the evaluation criteria of the flow velocity reduction formulated by the velocity field distribution were applied to determine the variation rule

with varying parameters for the final optimal configuration. List of symbols and their units used in the present study are given in Table 1.

Table 1. Nomenclature.

Symbol	Description	Symbol	Description
a	blade radius (m)	P_{in}	power available in the water (W)
b	blade height (m)	P_{out}	power output of the turbine (W)
C_a	attenuation coefficient	u	instantaneous velocity (m/s)
C_m	torque coefficient (-)	U	incoming flow speed (m/s)
C_p	power coefficient (-)	TSR	Tip speed ratio (-)
d	overlap distance (m)	y^+	dimensionless wall distance (-)
D	turbine diameter (m)	ε	blade curvature (-)
D_0	endplate diameter (m)	θ	present turbine rotation angle ($^\circ$)
e	overlap ratio (-)	ρ	density of water (kg/m^3)
H	height of turbine (m)	ω	rotational speed (rad/s)
L	velocity reduction length (m)	CFD	computational fluid dynamics
L_a	relative attenuation length (-)	SHT	Savonius hydrokinetic turbine
M	turbine torque (N-m)	VMP	Velocity measurement probe
N	blade number (-)		

2. Geometry and Property Parameter Definitions

The parameters that commonly affect the hydrodynamic characteristics of a Savonius rotor, such as the overlap ratio between two blades and the number and shape of the blades, can also be considered as influencing factors when exploring the flow velocity reduction performance of an SHT. Figure 1 shows the schematic diagram of a rotating semicircle two- and three-bladed turbine. U is the incoming flow speed (m/s), N is the blade number, θ is the present turbine rotation angle, ω is the rotational speed (rad/s), a is the blade radius (m), D is the turbine diameter (m), and d is the overlap distance (m). The overlap ratio (e) and blade curvature (ε) are defined as follows:

$$e = \frac{d}{D}, \quad (1)$$

$$\varepsilon = \frac{b}{a}, \quad (2)$$

where d is the overlap distance (m), D is the turbine diameter (m), b is the blade height (m), a is the blade radius (m).

The energy capture efficiency of an SHT is generally evaluated by the power coefficient (C_p), torque coefficient (C_m), and TSR . The flow velocity reduction performance of an SHT is assessed by the attenuation coefficient (C_a) and the relative attenuation length (L_a), which are defined as follows:

$$TSR = \frac{\omega D}{2U}, \quad (3)$$

$$C_m = \frac{4M}{\rho U^2 D^2 H}, \quad (4)$$

$$C_p = \frac{P_{out}}{P_{in}} = \frac{2M\omega}{\rho H D U^3} = C_m \times TSR, \quad (5)$$

$$C_a = \frac{U - u}{U}, \quad (6)$$

$$L_a = \frac{L}{D}, \quad (7)$$

where ω is the rotational speed (rad/s), D is the turbine diameter (m), U is the incoming flow speed (m/s), M is the turbine torque (N-m), ρ is the fluid density (kg/m^3), H is the turbine height (m), P_{out} is the power output of the turbine (W), P_{in} is the power available in the water (W), u is instantaneous velocity (m/s), L velocity reduction length (m).

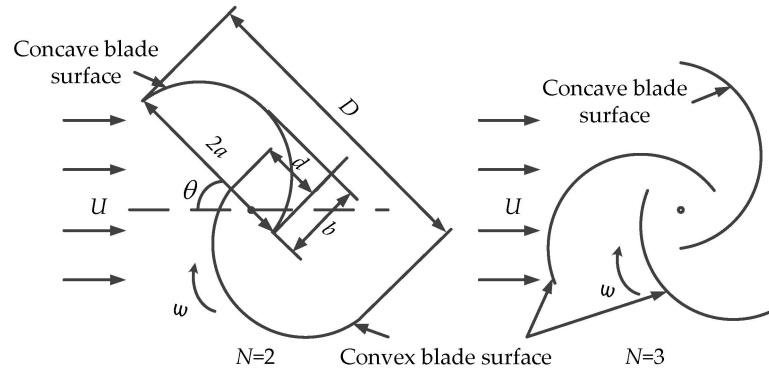


Figure 1. Operation schematic of an SHT.

3. Numerical Simulation

The wake flow of an SHT is particularly complex, due to the formation of many vortices around the rotating SHT. In this study, the CFD simulation software Star-CCM was used to investigate the flow field structure around the turbine. The turbine blades were symmetrical along the vertical axis, and the influence of the aspect ratio and end plate could be ignored in this study. Hence, the two-dimensional CFD numerical simulation was performed to study the properties of the SHT. This simulation strategy reduced the number of calculations without impacting the simulation accuracy.

3.1. Simulation Domain Size and Boundary Conditions

Sliding grid technology was adopted to simulate the rotation of the water turbine. As shown in Figure 2, the entire simulation domain was divided into two distinct regions: The stationary and rotation. The two regions were connected through the sliding interface. In order to avoid the boundary conditions influencing the simulation results, the size of the computational domain needed to be set to be sufficiently large. As shown in Figure 2, the simulation domain was $48D$ long and $10D$ wide, and the turbine was $8D$ away from the left boundary. The typical boundary conditions were also employed: The velocity inlet was set on the left boundary, and a velocity amplitude of 1.5 m/s was given. The right boundary was set as the pressure outlet, and the upper and lower boundaries were set as a symmetric plane. The turbine was set as a nonslip wall surface, as shown in Figure 2.

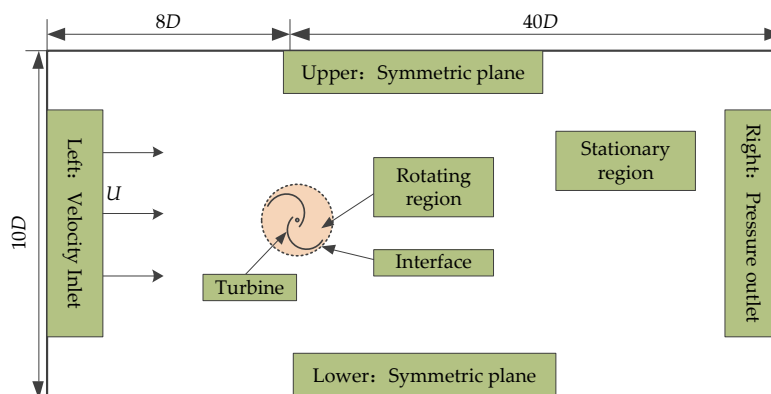


Figure 2. Computing domains and boundary conditions.

3.2. Meshing and Simulation Model Selection

The meshing of the computational domain is shown in Figure 3. The two regions were divided by two unstructured meshes. Hexahedral and trimmer meshes were applied in the rotation and stationary regions, respectively. To ensure the accuracy of the interpolation at the interface and to reduce the numerical transmission error, one prismatic layer was generated on both sides with the same dimension (shown in Figure 3d), and the mesh near the interface was encrypted (shown in Figure 3a). Due to the hydrodynamic characteristic and the wake flow field of the SHT being the main investigation objects, the mesh density around the blade and its large rear area were also augmented, as shown in Figure 3a,b. On the other hand, 10 prismatic layers were formed on the surface of the blades (shown in Figure 3c) to enhance the mesh quality and describe the boundary layer flow with sufficient precision. The first layer had a thickness of approximately 0.4 mm, with a growth rate of 1.05, and the wall y^+ value of the blade was limited to 10. To verify mesh independence, the thicknesses of the first layer of the wall were set to 0.4, 0.3, and 0.15 mm, respectively. The total numbers of corresponding grids were nearly 600,000, 850,000, and 1,500,000; however, the difference between the calculation results of the average power coefficient of the SHT ($TSR = 0.9$) was less than 2%. To reduce the amount of computation, the total number of computational domain grids was set to 600,000.

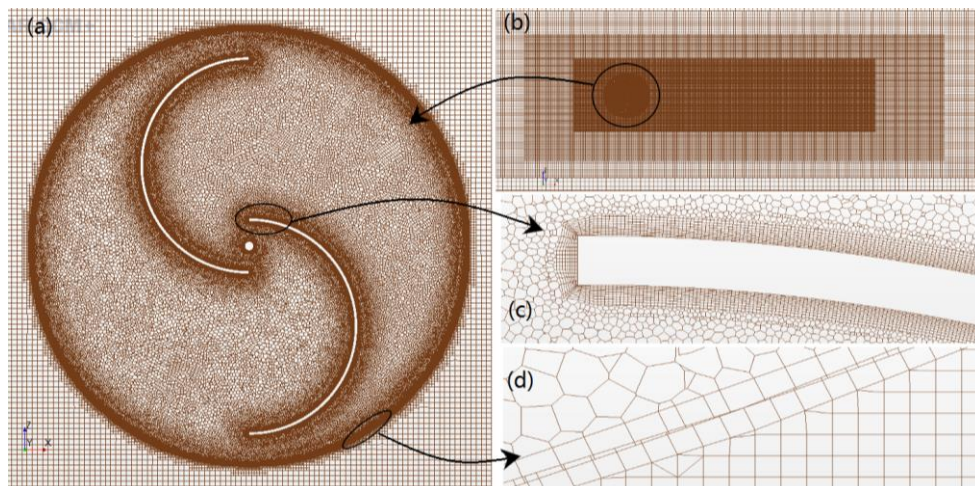


Figure 3. Mesh generation: (a) The rotating domain, (b) the whole domain, (c) mesh detail around the blade, and (d) one prismatic layer on the interface.

The Reynolds-Averaged Navier-Stokes (RANS) standard $k - \epsilon$ model was selected to simulate the turbulence, and the mixed wall-processing function was applied to realize the two-layer model. The momentum and turbulence of the governing equation adopted the second-order upwind scheme in spatial discretization. A first-order implicit format was assumed for time discretization with the maximum time step of 0.005 s, which ensured that the rotating angle of the turbine was less than 1° in one time step. The Semi-Implicit Method for Pressure-Linked Equations (SIMPLE) algorithm was used for numerical solution pressure-velocity coupling, for which each time step internal iteration was 50 times, and the residual convergence standard was 10^{-5} .

3.3. Simulation Validation

To verify the accuracy of the simulation model, the flow velocity reduction characteristics of the SHT were tested in a drag pool at the Ningbo Campus of Zhejiang University. The working section of the pool is 60 m long, 5 m wide, and 4 m deep. The maximum speed of the dragging system can reach 2.5 m/s. A semi-circular SHT with two blades was selected for the experiment, as shown in Figure 4a, and the specific parameters are shown in Table 2. An active measurement method was applied in this experiment to be consistent with the simulation. The turbine was driven by a servo

control system at a fixed speed, and the flow current was generated by dragging the rotor in stationary water. The overall experimental system is shown in Figure 4b, which is mainly composed of the battery power supply system, the servo motor drive system, the measurement system, the remote signal transmission system, and the control and data acquisition system. The velocity of the flow current was measured by a Vectrino Doppler velocimeter with a precision of 1 mm/s and a sampling frequency of 200 Hz, as shown in Figure 4c. In order to test the accuracy of the velocity monitoring probe in the wake field simulation, in this experiment, the velocimeter was placed at the position of a transverse distance of $1.5 D$ (the distance to the rotating center) and a longitudinal distance of $-0.12 D$ in the rear flow field of the SHT to measure the average velocity at different $TSRs$. The simulation results of the velocity monitoring probe at the same position are compared in Figure 5a. The trend of the two results obtained by the simulation and the experiment was generally similar. As the TSR increased, the speed attenuation coefficient rose initially and dropped after reaching the maximum value of around $TSR = 1.0$. However, the gap between the experimental and simulated values was obvious, perhaps due to the pulley guide rail of the dragging platform having a certain roughness and mechanical clearance caused by the velocimeter shaking with the running platform, producing measurement deflection. To enhance the computational efficiency of the simulation, turbulence was simulated by the RANS model, which also had an impact on the accuracy of the simulation results, especially in the high TSR range. Further, to test the hydrodynamic calculation reliability of the SHT, we adopted the same simulation method as above to calculate the C_p of the SHT. The experimental data of Parag K. Talukdar on the conventional semicircular double blade with an overlap ratio of 0.15 were compared with the simulation results. As shown in Figure 5b, although the simulation results were slightly lower than the results of Parag K. Talukdar's experiment, due to the 2D simulation not considering the effect of the end plate and aspect ratio, the trend of the two results was the same. Consequently, by comparing two sets of simulation and experimental data, the two-dimensional numerical simulation method adopted in this study was found to be feasible for the prediction of SHT properties.

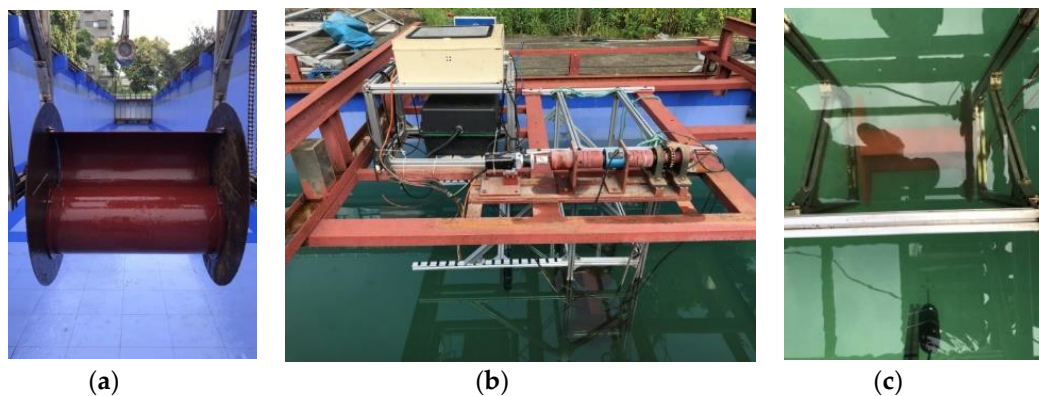


Figure 4. Experimental system: (a) The experimental SHT, (b) the overall system, and (c) the Vectrino Doppler velocimeter.

Table 2. Geometric parameters of the experiment Savonius turbine.

Parameter	Value
Number of blades (N)	2
Aspect ratio (H/D)	1.325
Overlap ratio (e)	0.11
Blade curvature (ϵ)	1
Rotor diameter (D)	0.36 m
Rotor height (H)	0.477 m
Endplate diameter (D_0)	0.52 m

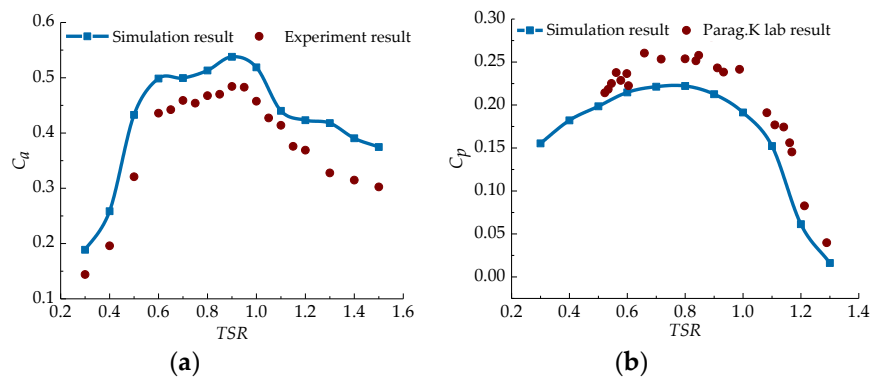


Figure 5. Comparisons between the simulated and experimental values: (a) The velocity attenuation coefficient (C_a) and (b) the power coefficient (C_p).

4. Results Analysis

4.1. Analysis of Flow Velocity Reduction Characteristics

To investigate the flow velocity reduction mechanism of the SHT, to summarize the variation law of the flow field, and to formulate the evaluation criteria of the flow velocity reduction characteristics, we studied the velocity field of the SHT under two operations: Stationary and rotating. The simulation model geometry parameters referenced Talukdar, P.k's [9] experimental optimal energy capture structure: A semicircular two-bladed turbine with an overlap rate of 0.15. When the turbine was under stationary operation, the θ was set to 90° , due to the blade's maximum upstream surface exerting the greatest influence on the flow field. When the blade rotated, the TSR was set to 0.9, due to the high energy-capture performance. From the comparison of the flow velocity profiles in the marked square regions at two states in Figure 6, the flow velocity reduction performance of the rotating SHT was obviously better than that of the stationary turbine. The marked square regions of Figure 6a show that the velocity field of the stationary SHT was unevenly distributed, and the flow velocity of many areas in the region was higher than 1.5 m/s. However, Figure 6b indicates that when the turbine rotated, the velocity profile in the wake was uniform, and the flow velocity of most of the region was less than 1.5 m/s. The streamline plotted in Figure 6 indicates that the SHT had a certain blocking impact on the incoming flow during both operations. When the turbine was stationary, the inlet flow affected by the vortex in the wake returned to the rear flow field with a higher speed, as shown in Figure 6a. It can be observed in Figure 6b that the incoming flow was circumvented from both sides when the turbine was rotating. Only a few fluid particles entered the rear flow field.

The flow velocity reduction mechanism of the SHT was revealed by comparing the velocity vector field around the turbine when it rotated to 90° and 180° with a TSR of 0.9. The velocity vector field, shown in Figure 7 reveals that there were many fluid particle motion collision zones (square areas). Especially in square area 1, the fluid particles ahead of the turbine driven by the rotating convex side moved in the direction perpendicular to the blade surface violently and crashed into the incoming flow, which was the main cause of the SHT's flow velocity reduction characteristic. In addition, the formation of vortices (circular areas) can be observed in Figure 7, such as the vortex (Figure 7b, circle 2) generated by the collision of the fluid particles (Figure 7a, square 2) and the vortex (Figure 7b, circle 3) that was created, due to the rotating structure of the turbine (Figure 7a, square 4). Observing the movement of the fluid particles affected by the vortices (Figure 7), it was found that the vortices always crashed into the fluid particles on both sides of the SHT, preventing them from entering its rear flow field and decreasing the velocity of fluid particles pushed by the rotating convex blade (the circular areas, shown in Figure 7). This also caused the gradually decreasing vortices to disappear (circle 1 in Figure 7a,b). This illustrates that the formation of vortices in the wake was another major factor that ensured that the turbine had good flow velocity reduction performance. The SHT flow velocity reduction was due to the following three factors: First, the concave surface had a direct blocking effect on the upstream

fluid. Second, in the rotating region of the SHT, the fluid particles pushed by the convex surface always collided with the upstream flow or the vortex in the wake. Third, the fluid particles on both sides of the SHT were prevented by the vortex from entering the wake zone.

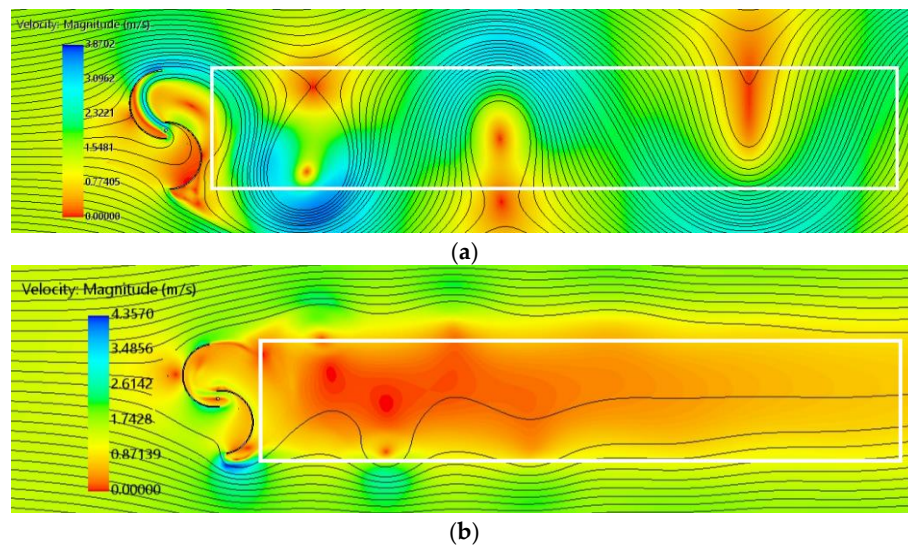


Figure 6. Velocity contours of the SHT with streamline: (a) Stationary stage ($\theta = 90^\circ$) and (b) rotating stage ($TSR = 0.9$).

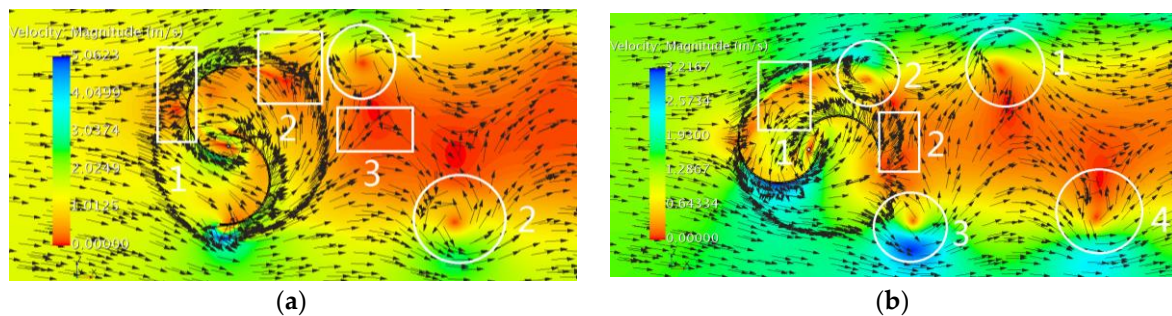


Figure 7. Velocity vectors of rotating Savonius turbine at $TSR = 0.9$. (a) The turbine rotates to $\theta = 90^\circ$; (b) The turbine rotates to $\theta = 180^\circ$.

In the simulation, 10 velocity measuring lines composed of a total of 70 velocity measurement probes (VMPs) were arranged behind the turbine, as shown in Figure 8. The specific horizontal distances of the 10 lines were 0.7, 1.4, 2.1, 2.8, 4.2, 5.6, 7, 10.15, 13.3, and 18.9 D (D is the diameter of the SHT) marked as L1–L10. The interval between the velocity measuring lines gradually grew larger with the increase in the distance from the turbine. Furthermore, each speed measuring line had a length of 1.5 D and evenly distributed seven VMPs marked as P1–P7. The curves of velocity with the time of several VMPs plotted in Figure 9 indicate that the velocity of a certain position in the wake periodically changed with a minor amplitude, especially in some areas with low velocity or that were far away from the turbine. Therefore, the average velocity value was acceptable for analyzing the velocity reduction property of the SHT.

The average value of each VMP at different $TSRs$ is given in Figure 10. When the TSR was 0.9, the velocities of most VMPs were below 1.5 m/s, and the minimum value of 0.2 m/s was reached at the position of L4P4 (Figure 10a). The values of a few VMPs were around 1.5 m/s, and the deceleration effect was not obvious. Therefore, the velocity attenuation coefficient in the effective flow velocity reduction region should be higher than 0.2 (the velocity was lower than 1.2 m/s). The variation of the curves in Figure 10a shows that, due to the influence of the external flow field and the formation and dissipation of vortices, on the horizontal direction from L1 to L10, the velocity of fluid particles

first decreased but then increased after achieving the minimum at L4. Observing the variation of the velocity of each VMP under the operation of the two different *TSRs*, as shown in Figure 10b,c, it is obvious that the average value of L4 was not the smallest. When $TSR = 0.5$ and 1.2 , the minimum values were obtained at L1 and L2, which illustrates that the position with the smallest average velocity among L1–10 changed under different *TSRs*. In the vertical direction from P1 to P7, Figure 10a shows that the velocity change trend of the VMPs in L1–10 was basically the same, and the minimum values were reached at P4. The fluid particles affected by the vortices crashed intensely around the midline of the SHT in the vertical direction, which resulted in a prominent performance reduction in this zone. In addition, the effective length of flow reduction at P4 extended the farthest to the horizontal distance of $15.1 D$. The effective length at other positions gradually decreased when they were far away from P4. In particular, the velocity of all VMPs at P7 was higher than 1.2 m/s ; thus, the domain below P6 was excluded from the effective flow reduction zone. Figure 11 shows the velocity contours with isolines at a particular time after periodic variation. The isolines of velocity, shown in Figure 11 reveal that the effective flow reduction zone of the SHT was “sword” shaped, which also confirms the rules of the velocity profile described above.

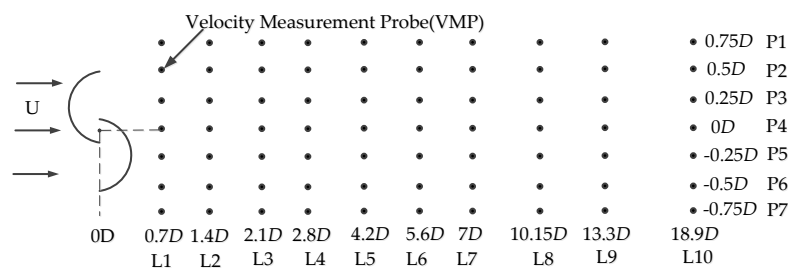


Figure 8. The distribution of VMPs in the wake of the SHT.

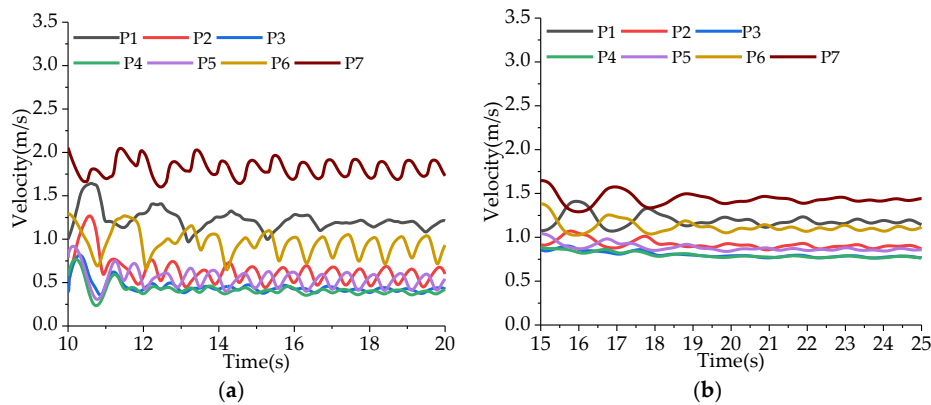


Figure 9. The instantaneous velocity of VMPs at different positions: (a) VMP in L5 and (b) VMP in L7.

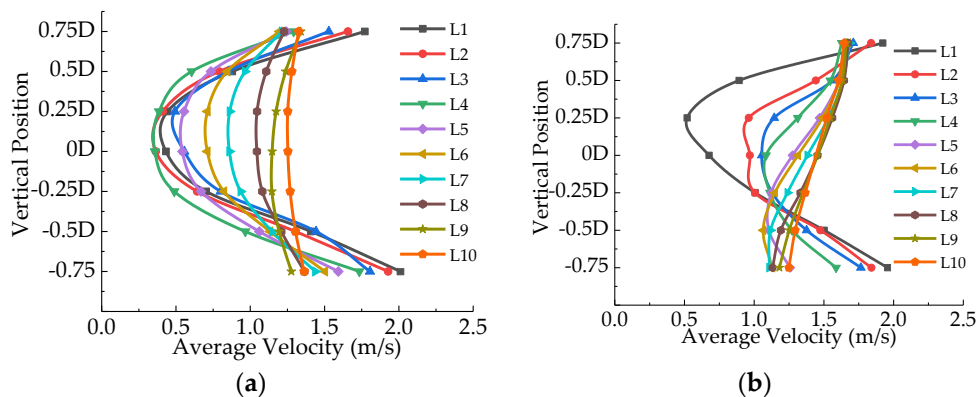


Figure 10. Cont.

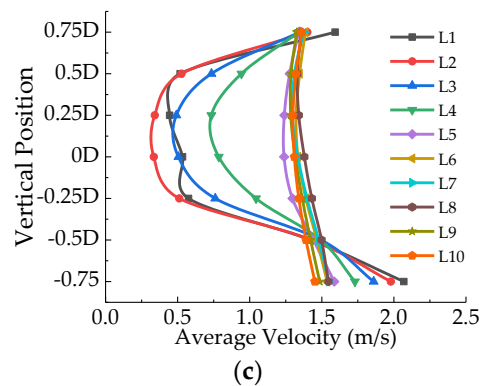


Figure 10. Average velocity of VMPs at different TSRs: (a) $TSR = 0.9$, (b) $TSR = 0.3$, and (c) $TSR = 1.5$

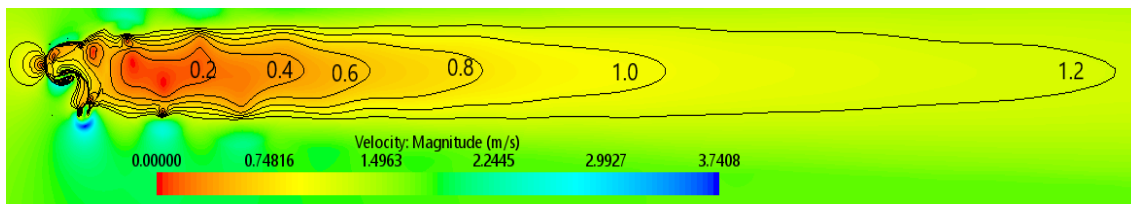


Figure 11. Velocity contours with isolines of Savonius turbine at $TSR = 0.9$.

In summary, considering the variation of the velocity profiles in the wake of the SHT in different TSR conditions, we defined the maximum average C_a in L1–L10 and horizontal L_a at $0D$ to evaluate the reduction strength and effective range of the SHT.

4.2. The Influence of TSR

Equation (5) shows that the C_p of the SHT turbine was determined by C_m and TSR . Based on the results reported earlier in this paper, it was found that TSR also had an effect on the flow velocity reduction characteristics. Therefore, studying the SHT properties of energy capture and flow velocity reduction at different $TSRs$ was essential. A two-blade semicircular SHT with an overlap ratio of 0.15 was selected as the object of analysis. The attenuation coefficient and relative attenuation length calculated by the reduction property evaluation rule are shown in Figure 10. The trend of C_a (Figure 12a) rose first and then dropped after reaching the maximum value of 0.696 at $TSR = 1.1$, but the C_a rose again with the further increase of TSR . The curve of L_a had two peaks, and the value of the higher peak was 15.1, obtained at $TSR = 0.9$. In addition, the power coefficient calculated by the simulation (Figure 12b) had a similar trend with the C_a , and the maximum value was obtained at $TSR = 0.9$. In the case of constant flow velocity, a larger TSR meant the faster rotational speed of the SHT. The movement of the fluid particles driven by the convex side was accelerated and collided with the fluid particles in the front, resulting in an improvement of flow velocity reduction performance. However, after the TSR rose to a particular extent, the blockage of the concave surface facing the fluid particles was weakened, and their speed was also higher, due to the effect of the convex side rotating backwards in turn to impact the flow velocity reduction property. Although the value of C_a was significant at a high TSR , the L_a and C_p were unacceptable. Otherwise, the C_p was available at a low TSR , but the performance of C_a and L_a were poor. Therefore, considering the above situation, the TSR operation range of the SHT of 0.6–1.2 was used for this study.

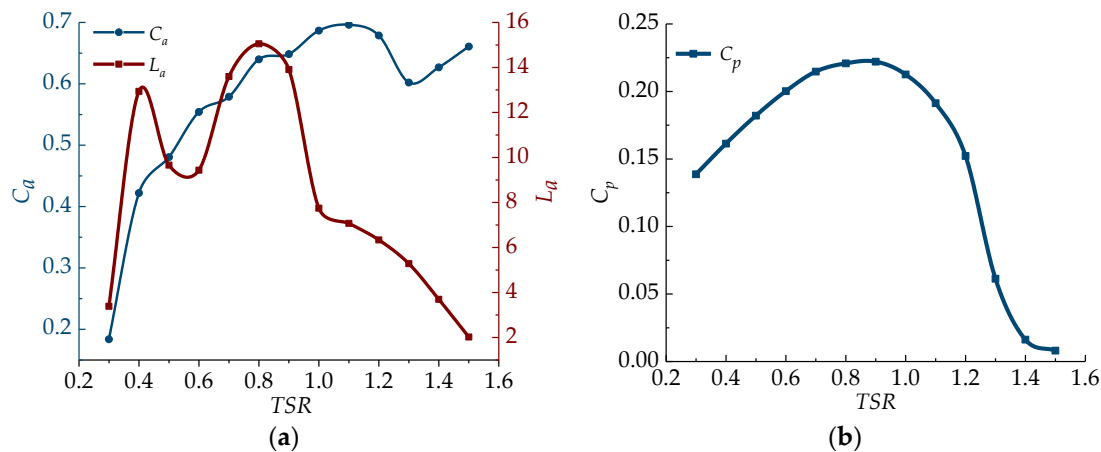


Figure 12. The influence of TSR on SHT properties for the case at $N = 2$, $e = 0.15$, and $\varepsilon = 1$: (a) The velocity attenuation coefficient (C_a) and relative attenuation length (L_a), and (b) the power coefficient (C_p).

4.3. The Influence of Blade Curvature (ε)

Blade curvature is the basic parameter that defines blade shape. In this study, three different blade curvatures ($\varepsilon = 1$, $\varepsilon = 0.8$, and $\varepsilon = 0.6$) were used to study their effect on SHT performance. The C_p , C_a , and L_a of these three types of the turbine are compared in Figure 13. The variation trends of each curve (Figure 13a) were similar; the C_a increased with the increase of the TSR, except for the curve of $\varepsilon = 1$, which dropped at the end. The comparison of the three curves clearly illustrates that the curvature of C_a was the best option, and the maximum value of 0.724 was obtained at $TSR = 1.2$. Figure 13b shows that the variation of L_a with the reduction of curvature had no obvious regularity. However, when the TSR was in the range of 0.8–1.2, the curvature of 1.0 performed well. The power capturing properties of the different curvatures are plotted in Figure 13c. It is obvious that $\varepsilon = 0.8$ was the best option, which is also confirmed by the experimental results of Parag k. Talukdar [9]. The mechanism of curvature affecting the flow velocity reduction performance can be explained by the velocity vector around the three types of SHT, as shown in Figure 14. A smaller curvature means a flatter blade shape, which leads to a more drastic collision between the fluid particles pushed by the convex side and the incoming flow. However, upon further reducing the curvature, the number of affected fluid particles decreases, as the decrease in blade surface size impacts the properties.

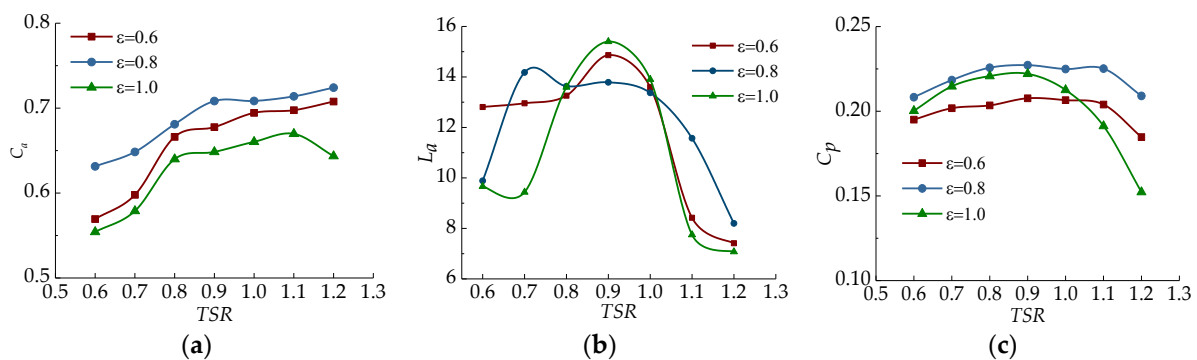


Figure 13. The influence of blade curvature on SHT properties for the case at $N = 2$ and $e = 0.15$: (a) The velocity attenuation coefficient (C_a), (b) the relative attenuation length (L_a), and (c) the power coefficient (C_p).

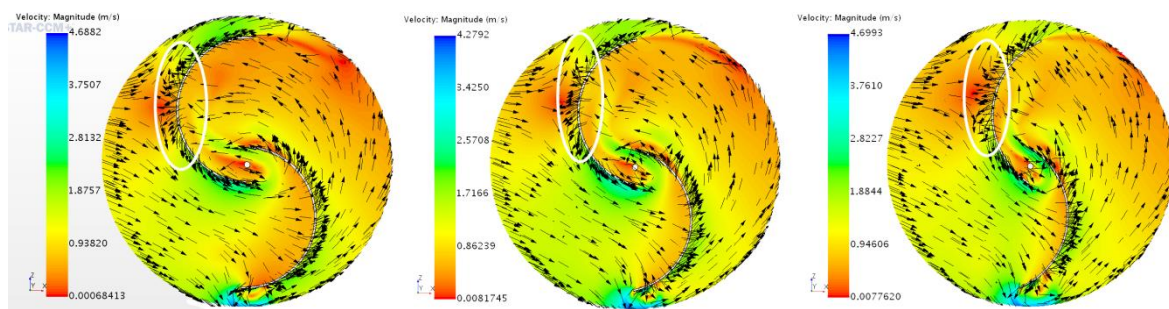


Figure 14. Flow visualization of the SHT rotating zone for different blade curvatures in the condition of $N = 2$, $e = 0.15$, and $TSR = 0.9$: (a) $\varepsilon = 1$, (b) $\varepsilon = 0.8$, and (c) $\varepsilon = 0.6$

4.4. The Influence of Overlap Ratio (e)

Overlap ratios (e) of 0, 0.15, and 0.3 of the SHT with the fixed parameters $N = 2$ and $\varepsilon = 1$ were selected as the research objects for analyzing the effect of the overlap ratio on turbine performance. The simulation results are plotted in Figure 15, where Figure 15 a–c describe the trend of C_a , L_a , and C_p in the case of three different overlap ratios, respectively. As shown in Figure 15a, although the curve of $e = 0$ was higher at $TSRs$ around 0.8 and 0.9, the curve of $e = 0.15$ had the best performance for the overall trend. Figure 15b shows that the trends of the L_a versus TSR curve at each overlap ratio were similar; however, the regularity of the L_a variation with the overlap ratio increase was not obvious. Further, $e = 0$ was better in the range between $TSR = 0.6$ and 0.8, while when the TSR continued to raise and was below 1.0, $e = 0.15$ was better. The power capture capacity is described in Figure 15c, which shows that the SHT had the best properties when the overlap ratio was 0.15. When the radius of rotation of the turbine remained the same, with the overlap ratio increasing slightly, the radius of the blade became larger, which had a positive effect on the reduction performance. However, with the further increase of the overlap ratio, the larger concave part was covered by the convex side, which impacted the direct blocking effect of the concave surface on the incoming fluid particles. Therefore, when the overlap ratio increased from 0 to 0.15, the turbine had better performance characteristics, but the properties degraded when the overlap ratio reached 0.3.

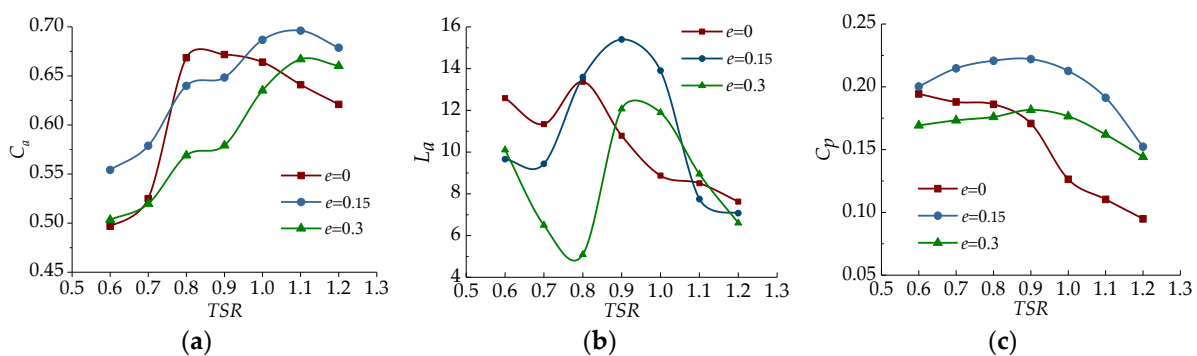


Figure 15. The influence of the overlap ratio on SHT properties for the case at $N = 2$ and $\varepsilon = 1$: (a) The velocity attenuation coefficient (C_a), (b) the relative attenuation length (L_a), and (c) the power coefficient (C_p).

4.5. The Influence of the Blade Number (N)

The simulations of the two-, three-, and four-bladed semicircular turbines with an overlap of 0.15 were carried out to study the effect of blade number on the performance of the SHT, and the calculation results are shown in Figure 16. The variation of the curves (Figure 16a) shows that the attenuation coefficient of the multiblade turbine was obviously higher than the two-bladed turbine, especially in the condition of low TSR . However, with the increase of TSR , the performance of the four-bladed turbine decreased sharply. As a result, the three-bladed performed best, for which the maximum C_a of 0.738 was obtained at $TSR = 1.1$. In addition, the L_a of the three types of turbine are given in Figure 16b.

The value of L_a in the case of the two-bladed turbine was obviously higher, and the same conclusion was obtained by comparing the C_p in Figure 16c. The vorticity contours of two- and three-bladed turbines at a particular orientation are shown in Figure 17. It is evident that, due to the increase in blade number, more fluid particles around the blades crashed into the incoming fluid, so more vortices were generated in the wake to enhance the velocity attenuation strength. However, with the increase in the number of vortices, the stability of the velocity field in the wake was also damaged, and more fluid particles on both sides of the turbine were driven by the vortices entering the rear flow field, which dampened the attenuation length.

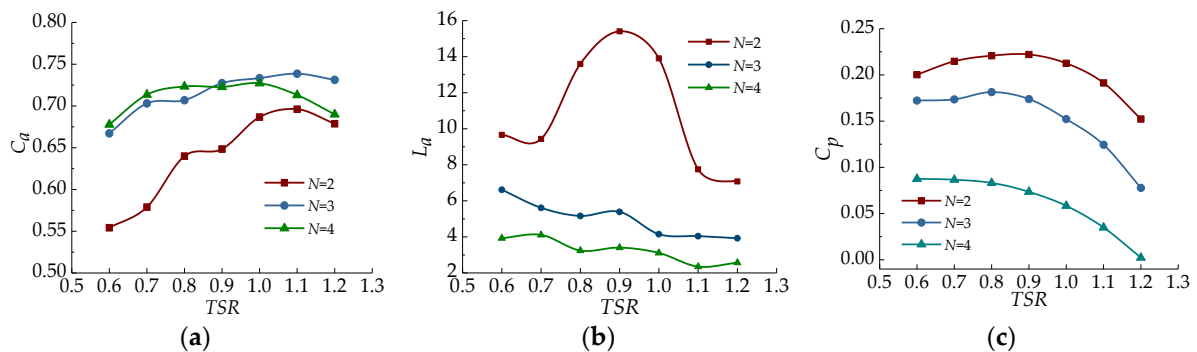


Figure 16. The influence of blade number on SHT properties for the case at $e = 0.15$ and $\varepsilon = 1$: (a) The velocity attenuation coefficient (C_a), (b) the relative attenuation length (L_a), and (c) the power coefficient (C_p).

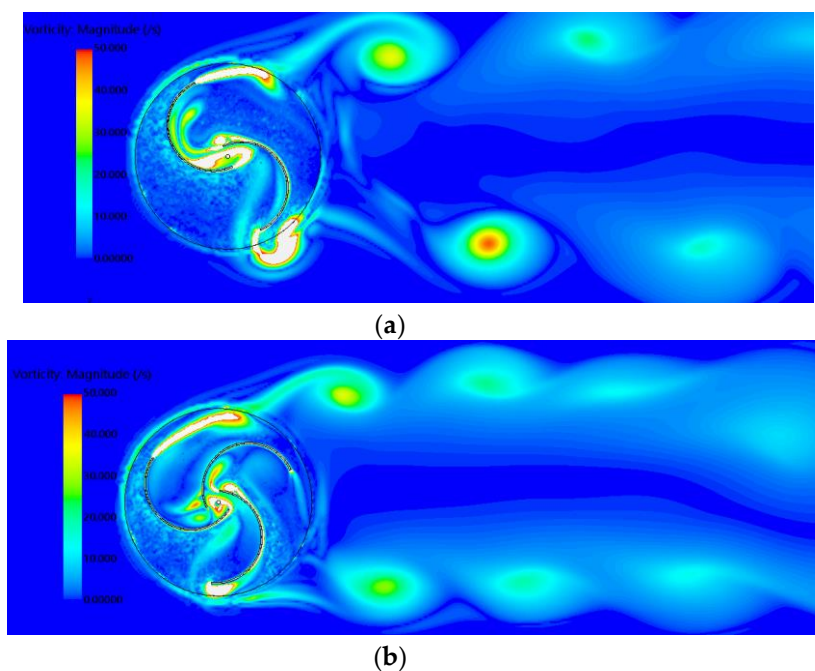


Figure 17. The vorticity contours of the SHT at different blade numbers in the conditions of $\varepsilon = 1$, $e = 0.15$, and $TSR = 0.9$: (a) $N = 2$ and (b) $N = 3$.

5. Discussion

The simulation results plotted in Figure 12 confirm that the optimum operational TSR is between 0.8 and 1.0. Regarding the best basic parameter configuration of the SHT considering the effect of flow velocity reduction, the C_p , C_a , and L_a of the SHT with different geometric structures at the optimum rotation TSR are compared in Table 3. The comparison of the different curvatures listed in the table demonstrates that the strength and efficiency of the flow velocity reduction and power capture are both

better at a curvature of 0.8, with improvements of 6.7% and 9.6% compared with the SHT presenting poorer performance. Although the maximum length of the flow velocity reduction was reached at $\varepsilon = 1$ with the value of 15.1, the increase from 13.8 obtained at $\varepsilon = 0.8$ was not obvious. Hence, the curvature of 0.8 is the optimal selection. The simulation results of different blade numbers (Table 3) show that the C_a had an approximately 10% increase from two blades to multiple blades, and the maximum C_a of 0.733 was obtained when the number of blades was four. However, the values of L_a and C_p reduced by about 65% and 35%, respectively, which drastically impacted the performance of the SHT; thus, the two-bladed turbine is recommended. For the different overlap ratios, the values of which are displayed in Table 2, when the overlap ratio was 0.15, the power capture was the most efficient, and it was 19% and 22% higher than the overlap ratio of 0 and 0.3, respectively. Comparing the attenuation coefficients, for the case of $e = 0$, the value (except for $TSR = 1.0$) was larger. However, in terms of the relative attenuation length, the length of $e = 0.15$ was completely longer than $e = 0$, and the maximum length increased by nearly 16%. Therefore, setting the overlap ratio at 0.15 is the best option.

Table 3. Max C_p , L_p and C_a of SHT at different parameters.

Parameters	Value	C_a	L_a	C_p	TSR
Curvature (ε)	$\varepsilon = 0.6$	0.669	13.25	0.203	0.8
		0.678	14.86	0.207	0.9
		0.694	13.59	0.206	1.0
	$\varepsilon = 0.8$	0.680	13.62	0.225	0.8
		0.709	13.78	0.227	0.9
		0.708	13.37	0.224	1.0
	$\varepsilon = 1.0$	0.639	13.59	0.221	0.8
		0.647	15.10	0.228	0.9
		0.660	13.90	0.212	1.0
Overlap (e)	$e = 0$	0.667	13.37	0.186	0.8
		0.671	10.78	0.171	0.9
		0.663	8.87	0.126	1.0
	$e = 0.15$	0.639	13.59	0.221	0.8
		0.647	15.1	0.228	0.9
		0.660	13.90	0.212	1.0
	$e = 0.3$	0.568	5.08	0.176	0.8
		0.579	12.06	0.181	0.9
		0.634	11.89	0.176	1.0
Blade (N)	$N = 2$	0.639	13.59	0.221	0.8
		0.647	15.1	0.228	0.9
		0.660	13.90	0.212	1.0
	$N = 3$	0.706	5.16	0.145	0.8
		0.726	5.38	0.138	0.9
		0.733	4.15	0.121	1.0
	$N = 4$	0.722	3.24	0.082	0.8
		0.722	3.40	0.072	0.9
		0.726	3.10	0.058	1.0

6. Conclusions

In this study, we conducted a parametric analysis of an SHT based on the number of blades, the blade shape, and the overlap ratio, considering the effect of flow velocity reduction. Two-dimensional simulations, verified by a water pool experiment, were performed to determine the varying regularity of the flow field. Power coefficient, attenuation coefficient and relative attenuation length have been calculated to evaluate the effect of design parameters on the SHT capacities of the power capture and flow velocity reduction. From this study, the following conclusions may be drawn:

(1) The computational results clearly show that the SHT had excellent flow velocity reduction performance in the sword-shaped zone behind it, due to the effects of obstructions, collisions,

and vortices in the wake generated by the rotating blade working on the incoming fluid particles. The maximum C_a of 0.733 and L_a of 15.1 can be reached at the specific design parameters.

(2) The velocity profiles in the effective area were relatively regular: The field around the P4 has a better flow velocity reduction property, but as the distance from the turbine increased, the reduction performance gradually decreased.

(3) Among the parameters, the TSR had the most obvious effect on the properties of the SHT, and the optimal TSR working range was found to be between 0.8 and 1.0.

(4) The results analysis indicates that the TSR , overlap ratio, and blade curvature have the same trend of effects on the flow velocity reduction and energy capture characteristics, but the blade number does not. This fact implies that the improvement of flow velocity reduction by optimizing parameters will not reduce the SHT power generation efficiency.

(5) Considering the effect and efficiency of flow velocity reduction and energy capture comprehensively, a double-bladed SHT with an overlap ratio of 0.15 and a blade curvature of 0.8 is the optimal configuration. The maximum values of C_a , L_a , and C_p of the SHT are 0.709, 13.78, and 0.227, respectively.

Author Contributions: Conceptualization, J.Y. and F.L.; methodology, F.L. and Z.Y.; software, F.L. and Z.Y.; validation, J.Y. and J.C.; formal analysis, F.L., Z.Y. and J.C.; investigation, F.L.; resources, J.Y. and J.C.; data curation, J.Y. and W.M.; writing—original draft preparation, F.L.; writing—review and editing, F.L.; visualization, F.L.; supervision, J.C.; project administration, J.Y. and J.C.; funding acquisition, J.Y. and J.C. All authors have read and agreed to the published version of the manuscript.

Funding: This research was funded by the Natural Science Foundation of Heilongjiang Province of China, grant number E2018019 and the Fundamental Research Funds for the Central Universities, grant number HEUCFP201733 and HEUCFP201814.

Conflicts of Interest: The authors declare no conflict of interest.

References

1. Liu, H.W.; Ma, S.; Li, W.; Gu, H.G.; Lin, Y.G.; Sun, X.J. A review on the development of tidal current energy in China. *Renew. Sustain. Energy Rev.* **2011**, *15*, 1141–1146. [[CrossRef](#)]
2. Savonius, S.J. The S-rotor and its applications. *Mech. Eng.* **1931**, *53*, 333–338.
3. Kumar, A.; Saini, R.P. Performance parameters of Savonius type hydrokinetic turbine—A Review. *Renew. Sustain. Energy Rev.* **2016**, *64*, 289–310. [[CrossRef](#)]
4. Akwa, J.V.; Vielmo, H.A.; Petry, A.P. A review on the performance of Savonius wind turbines. *Renew. Sustain. Energy Rev.* **2012**, *16*, 3054–3064. [[CrossRef](#)]
5. Tummala, A.; Velamati, R.K.; Sinha, D.K.; Indrajaya, V.; Krishna, V.H. A review on small scale wind turbines. *Renew. Sustain. Energy Rev.* **2016**, *56*, 1351–1371. [[CrossRef](#)]
6. Cao, L.; Wang, W.; Yang, Y.; Yang, C.; Yuan, Z.; Xiong, S.; Diana, J. Environmental impact of aquaculture and countermeasures to aquaculture pollution in China. *Environ. Sci. Pollut. Res.* **2007**, *14*, 452–462. [[CrossRef](#)]
7. Zhao, Y.P.; Bai, X.D.; Dong, G.H.; Bi, C.W.; Gui, F.K. Numerical analysis of the elastic response of a floating collar in waves. *Ocean Eng.* **2015**, *95*, 175–182. [[CrossRef](#)]
8. Lader, P.F.; Enerhaug, B. Experimental investigation of forces and geometry of a net cage in uniform flow. *IEEE J. Ocean. Eng.* **2005**, *30*, 79–84. [[CrossRef](#)]
9. Talukdar, P.K.; Sardar, A.; Kulkarni, V.; Saha, U.K. Parametric analysis of model Savonius hydrokinetic turbines through experimental and computational investigations. *Energy Convers. Manag.* **2018**, *158*, 36–49. [[CrossRef](#)]
10. Saha, U.K.; Thotla, S.; Maity, D. Optimum design configuration of Savonius rotor through wind tunnel experiments. *J. Wind Eng. Ind. Aerodyn.* **2008**, *96*, 1359–1375. [[CrossRef](#)]
11. Tian, W.; Song, B.; Mao, S. Numerical investigation of a Savonius wind turbine with elliptical blades. *Proc. CSEE* **2014**, *34*, 5796–5802. [[CrossRef](#)]
12. Kamoji, M.A.; Kedare, S.B.; Prabhu, S.V. Performance tests on helical Savonius rotors. *Renew. Energy* **2009**, *34*, 521–529. [[CrossRef](#)]

13. Kumar, A.; Saini, R.P. Performance analysis of a single stage modified Savonius hydrokinetic turbine having twisted blades. *Renew. Energy* **2017**, *113*, 461–478. [[CrossRef](#)]
14. Tian, W.; Song, B.; VanZwieten, J.; Pyakurel, P. Computational fluid dynamics prediction of a modified savonius wind turbine with novel blade shapes. *Energies* **2015**, *8*, 7915–7929. [[CrossRef](#)]
15. Kerikous, E.; Thevenin, D. Optimal shape of thick blades for a hydraulic Savonius turbine. *Renew. Energy* **2019**, *134*, 629–638. [[CrossRef](#)]
16. Golecha, K.; Eldho, T.I.; Prabhu, S.V. Influence of the deflector plate on the performance of modified Savonius water turbine. *Appl. Energy* **2011**, *88*, 3207–3217. [[CrossRef](#)]
17. Irabu, K.; Roy, J.N. Characteristics of wind power on Savonius rotor using a guide-box tunnel. *Therm. Fluid Sci.* **2007**, *32*, 580–586. [[CrossRef](#)]
18. Tartuferi, M.; D'Alessandro, V.; Montelpareb, S.; Ricci, R. Enhancement of Savonius wind rotor aerodynamic performance: A computational study of new blade shapes and curtain systems. *Energy* **2015**, *79*, 371–384. [[CrossRef](#)]
19. Yao, Y.X.; Tang, Z.P.; Wang, X.W. Design based on a parametric analysis of a drag driven VAWT with a tower cowling. *J. Wind Eng. Ind. Aerodyn.* **2013**, *116*, 32–39. [[CrossRef](#)]
20. Ostos, I.; Ruiz, I.; Gajic, M.; Gómez, W.; Bonilla, A.; Collazos, C. A modified novel blade configuration proposal for a more efficient VAWT using CFD tools. *Energy Convers. Manag.* **2019**, *180*, 733–746. [[CrossRef](#)]
21. Gupta, R.; Biswas, A.; Sharma, K.K. Comparative study of a three-bucket Savonius rotor with a combined three-bucket Savonius–three-bladed Darrieus rotor. *Renew. Energy* **2008**, *33*, 1974–1981. [[CrossRef](#)]



© 2019 by the authors. Licensee MDPI, Basel, Switzerland. This article is an open access article distributed under the terms and conditions of the Creative Commons Attribution (CC BY) license (<http://creativecommons.org/licenses/by/4.0/>).